Chinese Journal of Aeronautics, (2016), 29(3): 675–687

Chinese Society of Aeronautics and Astronautics
& Beihang University

Chinese Journal of Aeronautics

cja@buaa.edu.cn
www.sciencedirect.com

Nonlinear dynamic modeling of a helicopter planetary gear train for carrier plate crack fault diagnosis

Fan Lei [a,b], **Wang Shaoping** [a,*], **Wang Xingjian** [a], **Han Feng** [b], **Lyu Huawei** [b]

[a] *School of Automation Science and Electrical Engineering, Beihang University, Beijing 100083, China*
[b] *41th Detachment, People's Liberation Army Troop 61267, Beijing 101114, China*

Received 23 July 2015; revised 22 October 2015; accepted 24 January 2016
Available online 10 May 2016

KEYWORDS

Angular shift;
Carrier plate crack;
Crack fault diagnosis;
Helicopter planetary gear train;
Nonlinear dynamics modeling

Abstract Planetary gear train plays a significant role in a helicopter operation and its health is of great importance for the flight safety of the helicopter. This paper investigates the effects of a planet carrier plate crack on the dynamic characteristics of a planetary gear train, and thus finds an effective method to diagnose crack fault. A dynamic model is developed to analyze the torsional vibration of a planetary gear train with a cracked planet carrier plate. The model takes into consideration nonlinear factors such as the time-varying meshing stiffness, gear backlash and viscous damping. Investigation of the deformation of the cracked carrier plate under static stress is performed in order to simulate the dynamic effects of the planet carrier crack on the angular displacement of carrier posts. Validation shows good accuracy of the developed dynamic model in predicting dynamic characteristics of a planetary gear train. Fault features extracted from predictions of the model reveal the correspondence between vibration characteristic and the conditions (length and position) of a planet carrier crack clearly.

1. Introduction

The planetary or epicyclic gear trains are widely used in aeronautical and industrial applications, because of their significant advantages including compact structure, self-centering capability and high power density. They are usually used at the final stages of helicopter main transmissions with their output directly connected to the main rotor shafts, and their reliability is of vital importance to helicopter operation.

In 2002, fatigue cracks were found in the planet carriers of two helicopter main transmissions (UH-60A, 2400 Series).[1] Cracks resulted in flight restrictions on a significant number of US Army UH-60A helicopters and the corresponding research on methods to diagnose this type of fault.[2–4] Data provided by maintenance technicians in China[5] also showed a high trend of similar failures in certain helicopters.

* Corresponding author. Tel.: +86 10 82338933.
E-mail addresses: leifan@buaa.edu.cn (L. Fan), shaopingwang@vip.sina.com (S. Wang).

Peer review under responsibility of Editorial Committee of CJA.

Production and hosting by Elsevier

http://dx.doi.org/10.1016/j.cja.2016.04.008

Nomenclature

θ	Torsional angular displacement
$\dot{\theta}$	Torsional angular velocity
$\ddot{\theta}$	Torsional angular acceleration
ω	Angular velocity
r	Radius
d	Diameter
a	Center distance/amplitude
α	Pitch circle pressure angle
α_m	Meshing angle
m_z	Module of gear
x	Linear displacement along the meshing line
X	Relative linear displacement along the meshing line
K	Elastic engagement force
C	Viscous damping force
T	Torque/time period
m	Mass
z	Number of teeth
f	Frequency
I	Mass moment of inertia
i	Gear ratio
t	Time
B	Half of backlash (clearance)
k	Gear mesh stiffness
c	Gear mesh damping coefficient
b	Gear face width
e	Integrated errors during engagement
μ	Crack fault condition coefficient
τ	Dimensionless time
ε	The tooth contact damping ratio
γ	Gear face contact ratio
k'	Stiffness of single tooth pair

Subscripts

s	Sun gear
r	Ring gear
i	Planet gear index ($i = 1, 2, 3, 4, 5$)
c	Carrier plate
sp$i$	Gear pair of sun gear/planet gear pi
rp$i$	Gear pair of ring gear/planet gear pi
pi	ith planet gear
a	Amplitude
b	Base circle
e	Equivalent value
D	Dive
L	Load
m	With respect to meshing
sc	Sun gear with respect to carrier plate
γ	On the unit tooth width
f	Crack fault
0	Standard values used in the dimensionless process
s-c	Sun gear rotation with respect to carrier
p-c	Planet gear rotation with respect to carrier
pp	Planet-pass
post 1	Post 1 on the carrier plate

Superscripts

$\dot{x}$	Derivative with respect to time
$\ddot{x}$	The second derivative with respect to time
$\bar{x}$	Dimensionless quantity
r	In a transmission ratio, it means a stationary ring gear
ϕ_0	Spacing angle of the planetary gear train, $\phi_0 = 2\pi/N$

Vibration is the key for diagnosis of cracks in the helicopter transmission. Using the vibration signal for investigating the cracked transmissions addresses two aspects.[6–8] The first one is the effects of cracks on the structural dynamic characteristics such as natural frequencies and mode shape of damaged transmissions as a "direct problem" and the second one is how to predict the location and size of the cracks from the measured information of the damaged transmissions as an "inverse problem". The direct analysis of vibrating transmissions in the presence of carrier plate cracks is basic and necessary to solve the inverse problem.

Over the years, a large number of researchers committed to solve the "inverse problem" and focused on vibration signal detection, acquisition, processing and analysis, searching for effective ways of diagnosing the cracked planetary transmission.[3,4,9–14] However, some results showed that the crack fault was detectable in ideal test-cell conditions, but coupled signals and noise from other rotating components can easily overshadow the effect of a cracked part, such as a cracked planet carrier, under airborne conditions, thus leading to a failed diagnosis.[1,4]

As to the "direct problem" of planetary gear train, researchers paid much more attention to its solution and have already obtained some significant results. McFadden and Smith[15] illustrated that different phases produced by the planet gears may cause asymmetry of the modulation sidebands about the tooth meshing frequency in planetary gear vibration. T. Sun et al.[16,17] established a torsional-lateral nonlinear vibration model and obtained the frequency response characteristics of a planetary gear train. Furthermore, Z. M. Sun et al.[18] investigated the influence of the parametric excitations on the dynamic responses and dynamic gear tooth loads, and proposed some useful suggestions on design and manufacture of planetary gear train. Alshyyab and Kahraman[19] proposed a discrete nonlinear torsional vibration model of a single-stage planetary train and investigated the influence of key gear design parameters on dynamic response. However, these studies are all based on the fault-free planetary gear train, although they proposed models including the time-varying meshing stiffness, clearance (backlash) nonlinearities as well as run-out errors, and analyzed the stability, bifurcation and chaos in planetary gear train vibration. Yuksel and Kahraman[20] employed a computational model of a planetary gear train to study the influence of surface wear on the dynamic behavior and indicated that surface wear had a significant influence on off-resonance speed ranges while its influence diminishes near

resonance peaks primarily due to tooth separations. Lei et al.[13] proposed two diagnostic parameters (the root mean square of the filtered signal (FRMS) and the normalized summation of positive amplitudes of the difference spectrum between the unknown signal and the healthy signal (NSDS)) based on the examination of the vibration characteristics in both time and frequency domains, for detecting and diagnosing tooth faults of planetary gearboxes. Cheng et al.[21] presented a physics-based model for the purpose of detecting sun gear tooth chipped damage in a 2K-H planetary gear train. Feng and Zuo[22] modeled the vibration signals of planetary gearboxes with gear damage, considering the amplitude modulation and frequency modulation (AMFM) effects induced by gear damage and time-varying conditions, as well as the effect of vibration transfer paths, then validated it with both experimental and industrial signals. Liang et al.[23] developed a crack propagation model and quantified the mesh stiffness reduction when a crack occurs in the sun gear or the planet gear. They also developed a planetary gear dynamic model to simulate the vibration signals of each gear and proposed a mathematical model to represent the effect of the transmission path aimed at detecting a cracked tooth in the sun gear.[24] These studies focus on the in-depth research on the effects of damaged gear tooth on the gear train dynamic characteristics. However studies on the influence of cracked planet carrier plate on a planetary gear train have been rarely reported. Patrick-Aldaco[25] developed a vibration signal model of the planetary gear train with a cracked carrier plate but failed to make the analysis to find its dynamic reasons, which will most likely reveal the effects of a cracked carrier plate.

Nevertheless, we noticed the fundamental difference between the dynamic characteristics of the two types of fault, cracked tooth of gears and cracked planet carrier plate, in the planetary gear train. The cracked gear tooth would be almost "quiet" except when it meshes with the teeth of another gear. However, the cracked carrier plate would be stimulated to release its effects in every single gear teeth meshing, which introduces many complex components into the planetary gear train vibration signals.

This paper aims to investigate the effects of a cracked planet carrier plate on the dynamic characteristics of a planetary gear train and to find the fault features to detect the crack fault. First, we propose a dynamic model to simulate the torsional vibration of a planetary gear train with a cracked planet carrier plate, considering nonlinear factors such as time-varying meshing stiffness, gear backlash and viscous damping. Additional angular shift obtained from deformation analysis under static stress is used to simulate the effects of a crack in the carrier plate. Then we validate the dynamic model with predictions of a multi-term harmonic balance method (MHBM) and a computational deformable-body model (CDM) and demonstrate its accuracy in predicting the dynamic characteristics of the gear train. Solving the differential equations numerically, we obtain sufficient fault features from amplitude variations of gears vibration, in both the time and frequency domains, which can be used to diagnose a carrier plate crack fault.

2. Model of planetary gear train

2.1. Torsional vibration model

The planetary gear train of a helicopter main transmission considered in this paper has a typical 2K-H structure (according to the Chinese classification), shown in Fig. 1. It consists of 4 types of key components, a sun gear (s), a stationary ring gear (r), a planet carrier (c), and N planet gears (pi, i = 1, 2, ..., N). Each planet gear is assembled on the carrier through a planet bearing (not visible in Fig. 1). Planet gears are free to rotate with respect to their mounting posts on the carrier, respectively. Each gear here is the involute spur gear.

The dynamic model of this system (shown in Fig. 2) employs a number of simplifying assumptions:

(1) The vibrations of the system are measured at a fixed point on the ring gear.
(2) Each gear body is assumed to be rigid and the flexibilities of the gear teeth at each gear mesh interface are modeled by a spring which has periodically time-varying stiffness acting along the gear line of action.
(3) Each gear and the planet carrier are assumed to move in the direction of torsion only (marked with the torsional angular displacement θ) and are not affected by axial forces.
(4) Viscous gear mesh damping elements are introduced to represent energy dissipation at the gear mesh.
(5) Gears and carrier are assumed to be free of any eccentricities or roundness errors.
(6) Planet gears are equally spaced along the circumference of the planet carrier and each planet gear has consistent kinetic parameters with others with fault free.

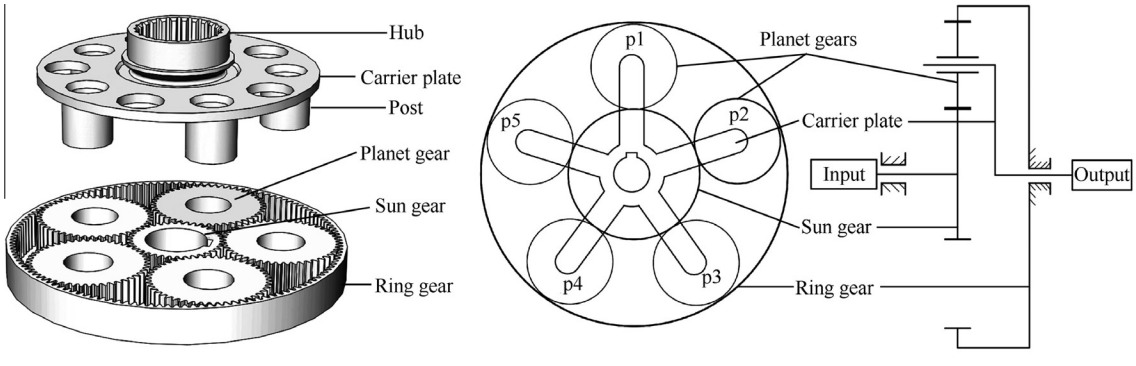

(a) Structure (b) Schematic diagram

Fig. 1 Structure and schematic diagram of a planetary gear train.

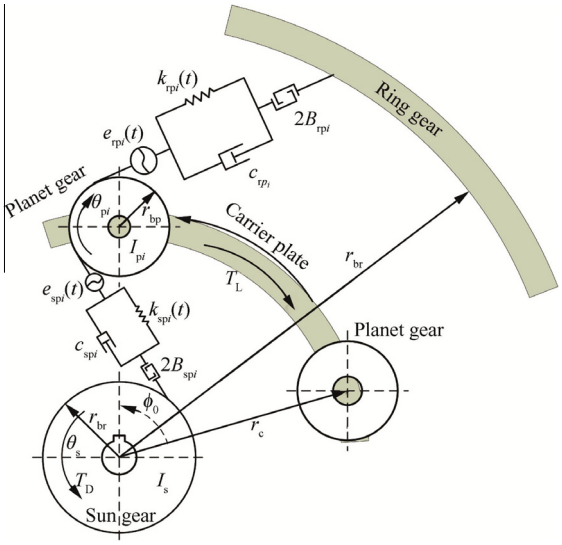

Fig. 2 Dynamic model of a planetary gear train.

In Fig. 2, the gear body j ($j = \mathrm{s}, \mathrm{r}, \mathrm{p}1, \mathrm{p}2, \cdots, \mathrm{p}N$) is modeled as a rigid disc with moment of inertia I_j, base radius r_{bj} and torsional angular displacement θ_j. Here θ_j is defined from the nominal rotation of the gear. Planet gears are located at radius r_c along a circumference with an identical spacing angles ϕ_0 ($\phi_0 = 2\pi/N$) between every two adjacent gears and are marked by index i ($i = 1, 2, \cdots, N$) in clockwise direction (top view). Also, $e_{spi}(t)$ and $e_{rpi}(t)$, which are applied along the line of action, represent comprehensive meshing errors resulting from gear manufacturing errors and assembling errors. B_{spi} and B_{rpi} represent the half of backlash in the sun/planet pair and ring/planet (or planet/ring) pair, respectively. The coefficients $k_{spi}(t)$ and $k_{rpi}(t)$ represent the time-varying meshing stiffness based on the linear spring model in two gear pairs (sun/plant and ring/plant) respectively, and, c_{spi} and c_{rpi} are the viscous damping effects.

External torque T_D, in the direction of sun gear rotation, is applied to the sun gear to represent input of the system, and T_L, in the opposite direction of carrier plate rotation, is applied to the carrier plate to represent output.

2.1.1. Transmission ratio

In this paper, i^r_{sc} is defined as the transmission ratio of the single stage planetary gear train with a stationary ring gear, an input sun gear and an output carrier plate. The transmission ratio of sun gear rotational speed n_s (r/min) and carrier plate rotational speed n_c (r/min) can be defined as

$$i^r_{sc} = \frac{n_s}{n_c} = \frac{z_s + z_r}{z_s} \tag{1}$$

where z_s is the sun gear teeth number and z_r the ring gear teeth number. The parameter i_{sp} is defined as the gear ratio of sun gear and planet gear,

$$i_{sp} = \frac{n_s}{n_p} = \frac{z_p}{z_s} \tag{2}$$

where n_p is the planet gear rotation speed (r/min) and z_p the number of planet gear teeth.

Table 1 Key frequencies of planetary gear train.

Component	Frequency (Hz)
Sun gear rotation	$f_s = n_s/60$
Carrier plate rotation	$f_c = n_c/60 = f_s/i^r_{sc}$
Sun gear rotation (with respect to carrier)	$f_{s-c} = f_s - f_c$
Planet gear rotation (with respect to carrier)	$f_{p-c} = f_{s-c}/i_{sp}$
Planet-pass	$f_{pp} = Nf_c$

2.1.2. Characteristic frequencies

The vibration of the planetary gear train is different from that of a fixed-axis gear train. As the planet carrier rotates, the sun/planet and ring/planet meshing points move all the time with respect to any vibration transducer mounted on the transmission housing. The vibration transmission paths consequently vary with respect to time.

In a single stage planetary gear train with a stationary ring gear, the two key gear pairs, sun/planet and ring/planet, have an identical meshing frequency, that equals the product of planet carrier rotating frequency f_c (Hz) and the number of ring gear teeth z_r, which reads

$$f_m = f_c z_r \tag{3}$$

The meshing angular velocity can be denoted as

$$\omega_m = 2\pi f_m \tag{4}$$

Other key frequencies are listed in Table 1

2.2. Derivation of equations of motion

Based on the Lagrange method (LM)[26], the equations of motion of the 2 + N degree freedom nonlinear dynamic model shown in Fig. 2 are as follows:

$$\begin{cases} I_s\ddot{\theta}_s + r_{bs}\sum_{i=1}^{N} c_{spi}\dot{x}_{spi} + r_{bs}\sum_{i=1}^{N} k_{spi}(t) f(x_{spi}, B_{spi}) = T_D \\ I_p\ddot{\theta}_{pi-c} + r_{bp}(c_{rpi}\dot{x}_{rpi} - c_{spi}\dot{x}_{spi}) + r_{bp}[k_{rpi}(t) f(x_{rpi}, B_{rpi}) \\ \quad -k_{spi}(t) f(x_{spi}, B_{spi})] = 0 \\ I_{cp}\ddot{\theta}_c - \sum_{i=1}^{N}(c_{spi}\dot{x}_{spi} r_{bs} + c_{rpi}\dot{x}_{rpi} r_{br}\cos\alpha) \\ \quad -\sum_{i=1}^{N}[k_{spi}(t) f(x_{spi}, B_{spi}) r_{bs} + k_{rpi}(t) f(x_{rpi}, B_{rpi}) r_{br}\cos\alpha] = -T_L \end{cases} \tag{5}$$

where $i = 1, 2, \cdots, N$, and I_s, I_p, and I_c are the equivalent moment of inertia of components and I_{cp} the equivalent moment of inertia of the carrier assembly.

$$\begin{cases} I_s = m_s r_{bs}^2 \\ I_p = m_p r_{bp}^2 \\ I_c = m_c r_c^2 \\ I_{cp} = I_c + NI_p + Nm_p r_c^2 \end{cases} \tag{6}$$

where θ_s and θ_c are the absolute rotation angles, and θ_{pi-c} is the relative rotation angle of planet gear pi with respect to the carrier.

The relative gear mesh linear displacements along the action lines, x_{spi} and x_{rpi}, are defined as

$$\begin{cases} x_{spi} = r_{bs}\theta_s - r_{bs}\theta_c - r_{bp}\theta_{pi-c} - e_{spi}(t) \\ x_{rpi} = r_{br}\theta_c - r_{bp}\theta_{pi-c} - e_{rpi}(t) \end{cases} \tag{7}$$

where $e_{spi}(t)$ and $e_{rpi}(t)$ are the comprehensive meshing errors of two gear pairs defined as

$$\begin{cases} e_{spi}(t) = E_{spi}\sin(\omega_m t + \varphi_{spi}) \\ e_{rpi}(t) = E_{rpi}\sin(\omega_m t + \varphi_{rpi}) \end{cases} \tag{8}$$

In Eq. (8), ω_m is the meshing angular velocity of planetary gear train, and E_{spi} and E_{rpi} are the amplitudes of the meshing errors, respectively.

2.2.1. Time-varying meshing stiffness

The time-varying meshing stiffness $k_{spi}(t)$ and $k_{rpi}(t)$ in Eq. (5) are periodic parametric excitations in two gear pairs, respectively. They have an identical angular frequency ω_m and can be written in Fourier series form as

$$\begin{cases} k_{spi}(t) = k_{sp} + \dfrac{2k_{as}}{\pi}\sin\omega_m t + \dfrac{2k_{as}}{3\pi}\sin 3\omega_m t + \dfrac{2k_{as}}{5\pi}\sin 5\omega_m t \quad i = 1,2,\cdots,N \\ k_{rpi}(t) = k_{rp} + \dfrac{2k_{ar}}{\pi}\sin\omega_m t + \dfrac{2k_{ar}}{3\pi}\sin 3\omega_m t + \dfrac{2k_{ar}}{5\pi}\sin 5\omega_m t \quad i = 1,2,\cdots,N \end{cases} \tag{9}$$

where k_{sp} and k_{rp} are the average meshing stiffness, which are defined as

$$\begin{cases} k_{sp} = (0.75\gamma + 0.25)k' b_s \\ k_{rp} = (0.75\gamma + 0.25)k' b_r \end{cases} \tag{10}$$

where b is gear face width, γ gear face contact ratio, and k' stiffness of single tooth pair.[27] k_{as} and k_{ar} are the stiffness amplitudes, and are defined as

$$\begin{cases} k_{as} = 0.5k_{sp} \\ k_{ar} = 0.5k_{rp} \end{cases} \tag{11}$$

2.2.2. Nonlinear gear backlash function

The nonlinear gear backlash functions, $f(x_{xpi}, B_{spi})$ and $f(x_{rpi}, B_{rpi})$ which are shown in Fig. 3, are defined as

$$f(x,B) = \begin{cases} x - B & x > B \\ 0 & -B \leqslant x \leqslant B \\ x + B & x < -B \end{cases} \tag{12}$$

where B is a half backlash of a gear pair.

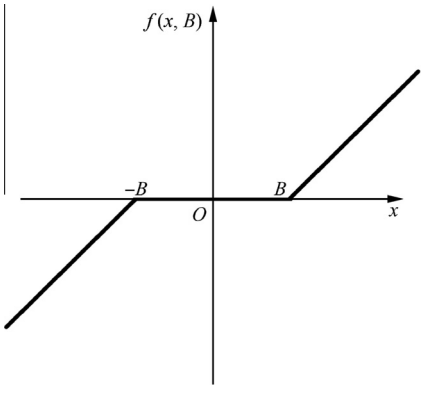

Fig. 3 Nonlinear gear backlash function.

2.2.3. Viscous damping coefficient

The viscous damping coefficients of engagement, c_{spi} and c_{rpi}, are defined as

$$\begin{cases} c_{spi} = 2\varepsilon\sqrt{\dfrac{k_{sp}m_s m_{pi}}{m_s + m_{pi}}} \\ c_{rpi} = 2\varepsilon\sqrt{k_{rp}m_{pi}} \end{cases} \tag{13}$$

where $\varepsilon \in [0.03, 0.17]$ is the tooth contact damping ratio.[28]

3. Model of planet carrier crack

3.1. Planet carrier crack fault

Fig. 4 shows the two fatigue cracks found in the planet carriers of two UH-60A helicopter main transmissions.[1] Similar faults were also found in a helicopter main transmission in China[5]

The feature of planet carrier crack fault can be described as follows:

(1) It is not a surface crack but a through-thickness crack in the carrier plate.
(2) The cracks are initiated in the planet post-to-plate radius on the side of forces.
(3) The cracks extend at both ends along the common tangents of the post circle and the hub circle. Under the worst circumstances, they may cause the hub-to-rim damages.

Fig. 5 illustrates a 145 mm crack in the planet carrier plate of a helicopter main transmission. Table 2 shows crack-free condition along with three other crack fault conditions in the planet carrier plate and the crack length l is obtained from the cracked carrier plates.

3.2. Deformation analysis under static stress

The carrier plate will respond to the action and reaction forces with localized deflections whether the planetary gear train operates with or without crack faults. A crack on the root of a planet gear mounting post of the planet carrier plate will reduce the local stiffness of that post. Apparently this reduction in stiffness will increase the deflection of the post when load is applied to the carrier plate. In order to investigate the dynamic characteristics of the cracked carrier plate under operational conditions, a static stress simulation is carried out by ANSYS® (ANSYS, Inc. Products 15.0). The conditions of static stress simulation are listed in Table 3 and the results are shown in Fig. 6.

The angular shift of each planet gear post, under unconstrained deformation condition, is calculated from both the forced and unforced conditions and highlighted in Fig. 7.

Table 4 shows the shift angles obtained through simulations. Post mounting numbering is the same as the planet gear index (clockwise, top view), and Post 1 is taken as the post where the crack locates.

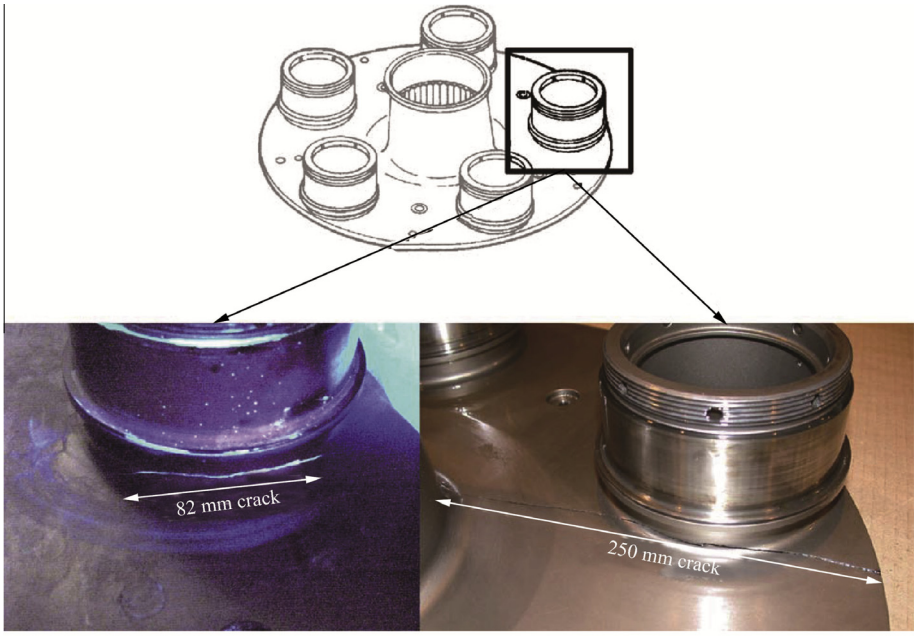

(a) 82 mm crack (b) 250 mm crack

Fig. 4 UH-60A planet carrier: 82 and 250 mm cracks[1] (Courtesy of ELSEVIER).

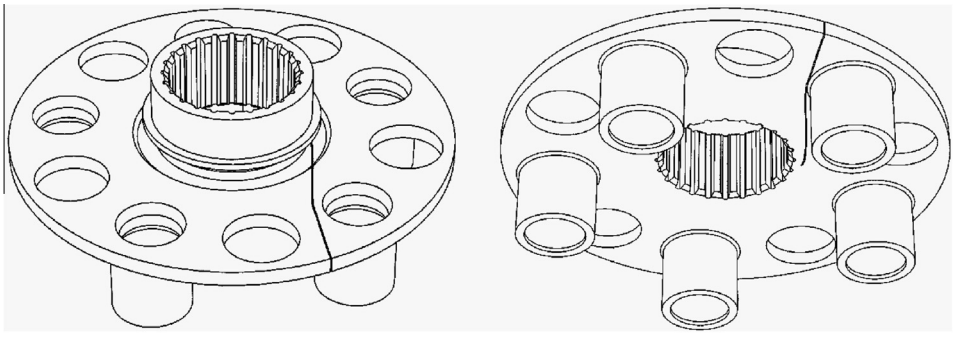

(a) Top view (b) Bottom view

Fig. 5 145 mm crack in a planet carrier plate.

Table 2 Conditions of a planet carrier crack fault.

View	Condition			
	Crack-free ($l = 0$ mm)	Mild (0 mm < $l \leqslant$ 0 mm)	Moderate (40 mm < $l \leqslant$ 85 mm)	Severe (85 mm < $l \leqslant$ 145 mm)
Top	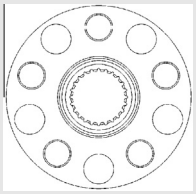	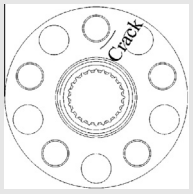	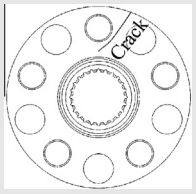	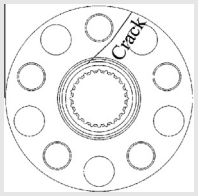
Bottom	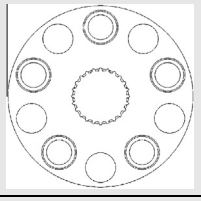	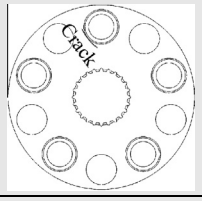	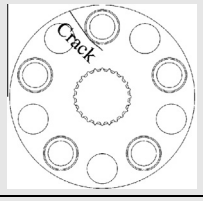	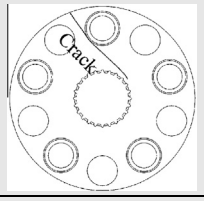

Table 3 Static stress simulation conditions.

Item	Content
Constraint	On the top of hub
Forces	5290 N at each post, tangential direction
Material	Structural steel
Crack length (mm)	0–145

The results of Table 4 are illustrated in Fig. 8, in which the dashed line shows a polynomial fitting curve of Post 1.

In Fig. 8, the static simulations of the carrier plate indicate that the shift angles do not vary linearly with respect to the crack length. Curve of Post 1 is sensitive to the crack length changes, while the others show narrow variations and no apparent regularity. Based on this observation and consideration of saving computational burden, a polynomial fitting curve is proposed to simulate the shift characteristic of Post 1, with shift angles of the others omitted.

The polynomial fitting equation is obtained as follows:

$$\begin{cases} a_{\mathrm{f}} = a_1 l^3 + a_2 l^2 + a_3 l \\ a_1 = 5.313 \times 10^{-7} \\ a_2 = -4.906 \times 10^{-5} \\ a_3 = 2.856 \times 10^{-3} \end{cases} \tag{14}$$

where a_{f} is defined as the shift angle amplitude function of Post 1, and a_1, a_2 and a_3 are the fitting parameters.

3.3. Modeling crack's dynamic effect

Based on above analysis, a dynamic shift angle function $\Delta\theta_{\mathrm{f}}$ is proposed to simulate the dynamic characteristics of Post 1 (the crack location) on a running and cracked carrier plate. As shown in Fig. 9, when the cracked carrier plate runs in a planetary gear train, Post 1 has an additional angular shift $\Delta\theta_{\mathrm{f}}$ besides the identical rotation angular displacement θ_{c} with the carrier plate and other posts, as given by

$$\theta_{\mathrm{post1}} = \theta_{\mathrm{c}} + \Delta\theta_{\mathrm{f}} \tag{15}$$

where $\Delta\theta_{\mathrm{f}}$ is a periodic function with the gear train meshing frequency ω_{m} due to the so-called breathing effect during the gear engagement and is defined as

$$\begin{aligned} \Delta\theta_{\mathrm{f}} &= a_{\mathrm{f}}\left[1 + \sin\left(\omega_{\mathrm{m}} t - \frac{\pi}{2}\right)\right] \\ &= \left(a_1 l^3 + a_2 l^2 + a_3 l\right)\left[1 + \sin\left(\omega_{\mathrm{m}} t - \frac{\pi}{2}\right)\right] \end{aligned} \tag{16}$$

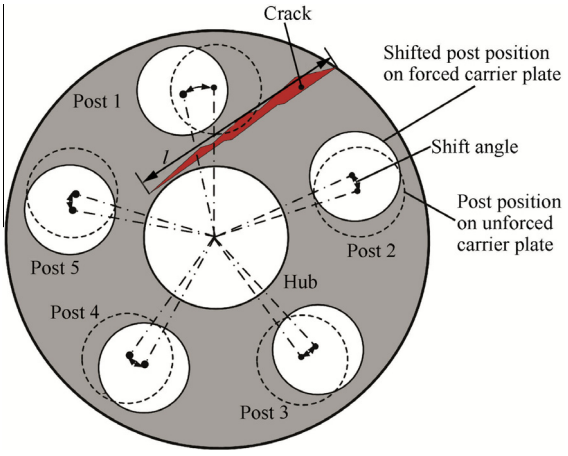

Fig. 7 Shift angles of posts caused by deformation of carrier plate (top view).

Table 4 Shift angles at each post with respect to unforced carrier plate.

Crack length (mm)	Shift angles at each post index (°)				
	1	2	3	4	5
0	0.17	0.17	0.17	0.17	0.17
11.15	0.18	0.17	0.18	0.17	0.16
22.30	0.19	0.17	0.18	0.17	0.16
33.45	0.21	0.17	0.18	0.17	0.15
44.60	0.23	0.17	0.18	0.16	0.15
55.75	0.28	0.18	0.19	0.16	0.13
66.90	0.30	0.18	0.19	0.16	0.12
78.05	0.32	0.18	0.19	0.16	0.12
89.20	0.41	0.18	0.21	0.15	0.09
100.35	0.53	0.18	0.23	0.14	0.06
111.50	0.57	0.18	0.24	0.13	0.05
122.65	0.64	0.18	0.25	0.13	0.03
133.80	1.07	0.26	0.29	0.06	0.01
145.00	1.12	0.27	0.30	0.06	0.01

Substituting Eq. (16) into Eqs. (7) and (5), we can obtain

$$\begin{cases} x_{\mathrm{sp1}} = r_{\mathrm{bs}}\theta_{\mathrm{s}} - r_{\mathrm{bs}}(\theta_{\mathrm{c}} + \Delta\theta_{\mathrm{f}}) - r_{\mathrm{bp}}\theta_{\mathrm{p1}} - e_{\mathrm{sp1}}(t) \\ x_{\mathrm{sp}i} = r_{\mathrm{bs}}\theta_{\mathrm{s}} - r_{\mathrm{bs}}\theta_{\mathrm{c}} - r_{\mathrm{bp}}\theta_{\mathrm{p}i} - e_{\mathrm{sp}i}(t) \\ x_{\mathrm{rp1}} = r_{\mathrm{br}}(\theta_{\mathrm{c}} + \Delta\theta_{\mathrm{f}}) - r_{\mathrm{bp}}\theta_{\mathrm{p1}} - e_{\mathrm{rp1}}(t) \\ x_{\mathrm{rp}i} = r_{\mathrm{br}}\theta_{\mathrm{c}} - r_{\mathrm{bp}}\theta_{\mathrm{p}i} - e_{\mathrm{rp}i}(t) \end{cases} \quad i = 2, 3, \cdots, N \tag{17}$$

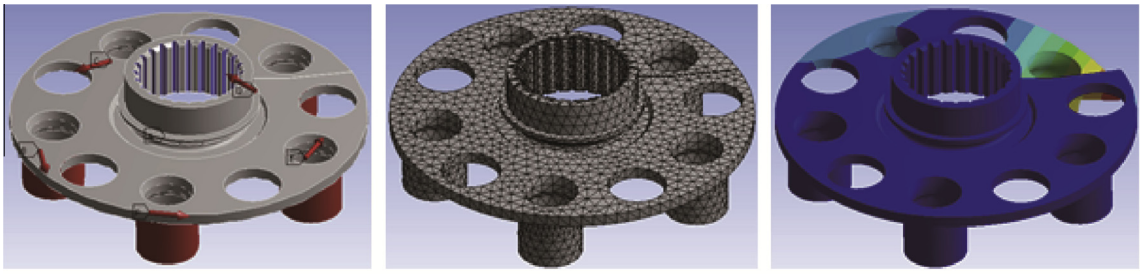

(a) Forces and constrains (b) Meshing grids (c) Deformation and displacment

Fig. 6 Deformation simulation under static stress.

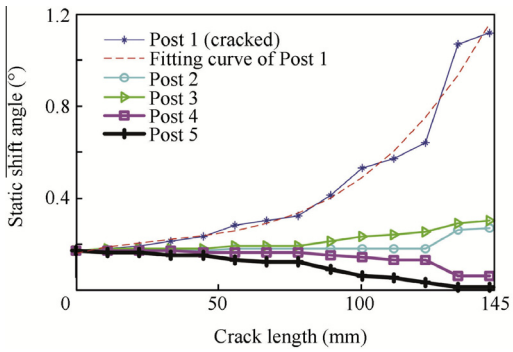

Fig. 8 Static shift angle curves at each post and fitting curve of Post 1.

$$
\begin{cases}
I_{\mathrm{s}}\ddot{\theta}_{\mathrm{s}}+\left[k_{\mathrm{sp1}}(t)f(x_{\mathrm{sp1}},B_{\mathrm{sp1}})+c_{sp1}\dot{x}_{sp1}\right]r_{\mathrm{bs}} \\
\quad+\sum_{i=2}^{N}\left[k_{\mathrm{sp}i}(t)f(x_{\mathrm{sp}i},B_{\mathrm{sp}i})+c_{\mathrm{sp}i}\dot{x}_{\mathrm{sp}i}\right]r_{\mathrm{bs}}=T_{\mathrm{D}} \\
I_{\mathrm{p1}}\ddot{\theta}_{\mathrm{p1}}-\left[c_{\mathrm{sp1}}\dot{x}_{\mathrm{sp1}}-c_{\mathrm{rp1}}\dot{x}_{\mathrm{rp1}}+k_{\mathrm{sp1}}(t)f(x_{\mathrm{sp1}},B_{\mathrm{sp1}})\right. \\
\quad\left.-k_{\mathrm{rp1}}(t)f(x_{\mathrm{rp1}},B_{\mathrm{rp1}})\right]r_{\mathrm{bp}}=0 \\
I_{\mathrm{p}i}\ddot{\theta}_{\mathrm{p}i}-\left[c_{\mathrm{sp}i}\dot{x}_{\mathrm{sp}i}-c_{\mathrm{rp}i}\dot{x}_{\mathrm{rp}i}+k_{\mathrm{sp}i}(t)f(x_{\mathrm{sp}i},B_{\mathrm{sp}i})\right. \\
\quad\left.-k_{\mathrm{rp}i}(t)f(x_{\mathrm{rp}i},B_{\mathrm{rp}i})\right]r_{\mathrm{bp}}=0 \qquad i=2,3,\cdots,N \\
I_{\mathrm{cp}}\ddot{\theta}_{\mathrm{c}}-r_{\mathrm{bs}}\left[(c_{\mathrm{sp1}}\dot{x}_{\mathrm{sp1}}+k_{\mathrm{sp1}}(t)f(x_{\mathrm{sp1}},B_{\mathrm{sp1}}))\right. \\
\quad\left.+\sum_{i=2}^{N}(c_{\mathrm{sp}i}\dot{x}_{\mathrm{sp}i}+k_{\mathrm{sp}i}(t)f(x_{\mathrm{sp}i},B_{\mathrm{sp}i}))\right] \\
\quad-r_{\mathrm{br}}\cos\alpha\left[(c_{\mathrm{rp1}}\dot{x}_{\mathrm{rp1}}+k_{\mathrm{rp1}}(t)f(x_{\mathrm{rp1}},B_{\mathrm{rp1}}))\right. \\
\quad\left.+\sum_{i=2}^{N}(c_{\mathrm{rp}i}\dot{x}_{\mathrm{rp}i}+k_{\mathrm{rp}i}(t)f(x_{\mathrm{rp}i},B_{\mathrm{rp}i}))\right]=-T_{\mathrm{L}}
\end{cases}
\tag{18}
$$

Substituting Eqs. (9), (12), and (17) into Eq. (18), a set of nonlinear algebraic equations are obtained:

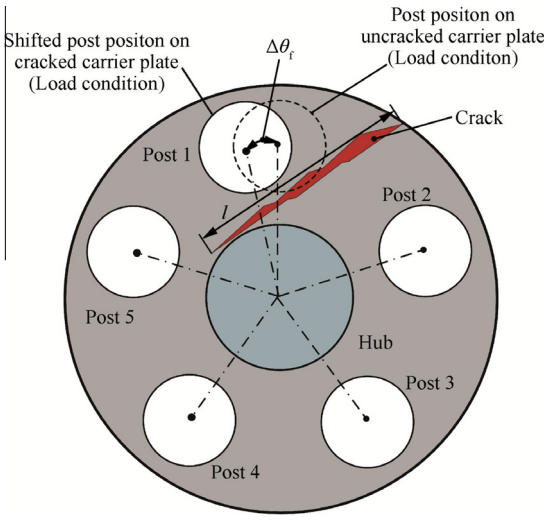

Fig. 9 Model of shift angle of Post 1 (top view).

Eq. (19) can be non-dimensionalized by using a characteristic length b_0 and a characteristic frequency ω_0 and by defining

$$
\begin{cases}
\omega_0=\frac{2\omega_{\mathrm{ns}}\omega_{\mathrm{nr}}}{\omega_{\mathrm{ns}}+\omega_{\mathrm{nr}}},b_0=B_{\mathrm{sp}i}=B_{rpi} \\
\tau=\omega_0 t,\bar{x}=\frac{x}{b_0} \\
m_{\mathrm{esp}}=\frac{m_{\mathrm{s}}m_{\mathrm{p}}}{m_{\mathrm{s}}+m_{\mathrm{p}}},m_{\mathrm{erp}}=m_{\mathrm{p}i} \\
\omega_{\mathrm{ns}}=\omega_{\mathrm{esp}}=\sqrt{k_{\mathrm{sp}}/m_{\mathrm{esp}}} \\
\omega_{\mathrm{nr}}=\omega_{\mathrm{erp}}=\sqrt{k_{\mathrm{rp}}/m_{\mathrm{erp}}} \\
k_{\mathrm{sp}}=\omega_{\mathrm{ns}}^2 m_{\mathrm{esp}},k_{\mathrm{rp}}=\omega_{\mathrm{nr}}^2 m_{\mathrm{erp}} \\
k_{\mathrm{s}}=\frac{k_{\mathrm{as}}}{k_{\mathrm{sp}}},k_{\mathrm{r}}=\frac{k_{\mathrm{ar}}}{k_{\mathrm{rp}}} \\
\bar{\omega}=\frac{\omega_m}{\omega_0}
\end{cases}
\tag{20}
$$

Then a set of dimensionless equations can be written as

$$
\begin{cases}
\ddot{x}_{\mathrm{sp1}} &= -\frac{r_{\mathrm{bs}}^2}{I_{\mathrm{s}}}\left[k_{\mathrm{sp1}}(t)f(x_{\mathrm{sp1}},B_{\mathrm{sp1}})+c_{\mathrm{sp1}}\dot{x}_{\mathrm{sp1}}\right]-\frac{r_{\mathrm{bs}}^2}{I_{\mathrm{s}}}\sum_{i=2}^{N}\left[k_{\mathrm{sp}i}(t)f(x_{\mathrm{sp}i},B_{\mathrm{sp}i})+c_{\mathrm{sp}i}\dot{x}_{\mathrm{sp}i}\right]+\frac{r_{\mathrm{bs}}T_{\mathrm{D}}}{I_{\mathrm{s}}} \\
&\quad-\frac{r_{\mathrm{bs}}^2}{I_{\mathrm{cp}}}\left[(c_{\mathrm{sp1}}\dot{x}_{\mathrm{sp1}}+k_{\mathrm{sp1}}(t)f(x_{\mathrm{sp1}},B_{\mathrm{sp1}}))+\sum_{i=2}^{N}(c_{\mathrm{sp}i}\dot{x}_{\mathrm{sp}i}+k_{\mathrm{sp}i}(t)f(x_{\mathrm{sp}i},B_{\mathrm{sp}i}))\right] \\
&\quad-\frac{r_{\mathrm{bs}}r_{\mathrm{br}}\cos\alpha}{I_{\mathrm{cp}}}\left[(c_{\mathrm{rp1}}\dot{x}_{\mathrm{rp1}}+k_{\mathrm{rp1}}(t)f(x_{\mathrm{rp1}},B_{\mathrm{rp1}}))+\sum_{i=2}^{N}(c_{\mathrm{rp}i}\dot{x}_{\mathrm{rp}i}+k_{\mathrm{rp}i}(t)f(x_{\mathrm{rp}i},B_{\mathrm{rp}i}))\right]+\frac{r_{\mathrm{bs}}T_{\mathrm{L}}}{I_{\mathrm{cp}}}-r_{\mathrm{bs}}\Delta\ddot{\theta}_{\mathrm{f}} \\
&\quad-\frac{r_{\mathrm{bp}}^2}{I_{\mathrm{p1}}}\left[c_{\mathrm{sp1}}\dot{x}_{\mathrm{sp1}}-c_{\mathrm{rp1}}\dot{x}_{\mathrm{rp1}}+k_{\mathrm{sp1}}(t)f(x_{\mathrm{sp1}},B_{\mathrm{sp1}})-k_{\mathrm{rp1}}(t)f(x_{\mathrm{rp1}},B_{\mathrm{rp1}})\right]-\ddot{e}_{\mathrm{sp1}}(t) \\
\ddot{x}_{\mathrm{rp1}} &= \frac{r_{\mathrm{br}}r_{\mathrm{bs}}}{I_{\mathrm{cp}}}\left[(c_{\mathrm{sp1}}\dot{x}_{\mathrm{sp1}}+k_{\mathrm{sp1}}(t)f(x_{\mathrm{sp1}},B_{\mathrm{sp1}}))+\sum_{i=2}^{N}(c_{\mathrm{sp}i}\dot{x}_{\mathrm{sp}i}+k_{\mathrm{sp}i}(t)f(x_{\mathrm{sp}i},B_{\mathrm{sp}i}))\right] \\
&\quad+\frac{r_{\mathrm{br}}^2\cos\alpha}{I_{\mathrm{cp}}}\left[(c_{\mathrm{rp1}}\dot{x}_{\mathrm{rp1}}+k_{\mathrm{rp1}}(t)f(x_{\mathrm{rp1}},B_{\mathrm{rp1}}))+\sum_{i=2}^{N}(c_{\mathrm{rp}i}\dot{x}_{\mathrm{rp}i}+k_{\mathrm{rp}i}(t)f(x_{\mathrm{rp}i},B_{\mathrm{rp}i}))\right]-\frac{r_{\mathrm{br}}T_{\mathrm{L}}}{I_{\mathrm{cp}}}+r_{\mathrm{br}}\Delta\ddot{\theta}_{\mathrm{f}} \\
&\quad-\frac{r_{\mathrm{bp}}^2}{I_{\mathrm{p1}}}\left[c_{\mathrm{sp1}}\dot{x}_{\mathrm{sp1}}-c_{\mathrm{rp1}}\dot{x}_{\mathrm{rp1}}+k_{\mathrm{sp1}}(t)f(x_{\mathrm{sp1}},B_{\mathrm{sp1}})-k_{\mathrm{rp1}}(t)f(x_{\mathrm{rp1}},B_{\mathrm{rp1}})\right]-\ddot{e}_{\mathrm{rp1}}(t)
\end{cases}
\tag{19}
$$

$$
\begin{cases}
\ddot{\bar{x}}_{\mathrm{sp1}}(\tau) &= -\left(\frac{Nr_{\mathrm{bs}}^2}{I_{\mathrm{s}}}+\frac{Nr_{\mathrm{bs}}^2}{I_{\mathrm{cp}}}+\frac{r_{\mathrm{bp}}^2}{I_{\mathrm{p1}}}\right)\frac{c_{\mathrm{sp1}}}{\omega_0}\dot{\bar{x}}_{\mathrm{sp1}}+\left(\frac{r_{\mathrm{bp}}^2}{I_{\mathrm{p1}}}-\frac{Nr_{\mathrm{bs}}r_{\mathrm{br}}\cos\alpha}{I_{\mathrm{cp}}}\right)\frac{c_{\mathrm{rp1}}}{\omega_0}\dot{\bar{x}}_{\mathrm{rp1}}\\
&\quad-\left(\frac{r_{\mathrm{bs}}^2}{I_{\mathrm{s}}}+\frac{r_{\mathrm{bs}}^2}{I_{\mathrm{cp}}}+\frac{r_{\mathrm{bp}}^2}{I_{\mathrm{p1}}}\right)\frac{\bar{k}_{\mathrm{sp1}}}{b_0\omega_0^2}(\tau)f(\bar{x}_{\mathrm{sp1}})+\left(\frac{r_{\mathrm{bp}}^2}{I_{\mathrm{p1}}}-\frac{r_{\mathrm{bs}}r_{\mathrm{br}}\cos\alpha}{I_{\mathrm{cp}}}\right)\frac{\bar{k}_{\mathrm{rp1}}}{b_0\omega_0^2}(\tau)f(\bar{x}_{\mathrm{rp1}})\\
&\quad-\left(\frac{(N-1)r_{\mathrm{bs}}^2}{I_{\mathrm{s}}}+\frac{(N-1)r_{\mathrm{bs}}^2}{I_{\mathrm{cp}}}\right)\frac{\bar{k}_{\mathrm{sp1}}}{b_0\omega_0^2}(\tau)f\left(\bar{x}_{\mathrm{sp1}}+\frac{r_{\mathrm{bs}}\Delta\theta_{\mathrm{f}}}{b_0}\right)-\frac{(N-1)r_{\mathrm{bs}}r_{\mathrm{br}}\cos\alpha}{I_{\mathrm{cp}}}\cdot\frac{\bar{k}_{\mathrm{rp1}}}{b_0\omega_0^2}(\tau)f\left(\bar{x}_{\mathrm{rp1}}-\frac{r_{\mathrm{br}}\Delta\theta_{\mathrm{f}}}{b_0}\right)\\
&\quad+\left(\frac{(N-1)r_{\mathrm{bs}}r_{\mathrm{br}}^2c_{\mathrm{rp1}}\cos\alpha}{I_{\mathrm{cp}}}-\frac{(N-1)r_{\mathrm{bs}}^3c_{\mathrm{sp1}}}{I_{\mathrm{cp}}}-\frac{(N-1)r_{\mathrm{bs}}^3c_{\mathrm{sp1}}}{I_{\mathrm{s}}}\right)\frac{\Delta\dot{\theta}_{\mathrm{f}}}{\omega_0^2}+\frac{r_{\mathrm{bs}}T_{\mathrm{D}}}{I_{\mathrm{s}}b_0\omega_0^2}+\frac{r_{\mathrm{bs}}T_{\mathrm{L}}}{I_{\mathrm{cp}}b_0\omega_0^2}-\frac{r_{\mathrm{bs}}\Delta\ddot{\theta}_{\mathrm{f}}}{\omega_0^2}-\frac{\ddot{e}_{\mathrm{sp1}}(\tau)}{\omega_0^2}\\
\ddot{\bar{x}}_{\mathrm{rp1}}(\tau) &= \left(\frac{Nr_{\mathrm{br}}r_{\mathrm{bs}}}{I_{\mathrm{cp}}}-\frac{r_{\mathrm{bp}}^2}{I_{\mathrm{p1}}}\right)\frac{c_{\mathrm{sp1}}}{\omega_0}\dot{\bar{x}}_{\mathrm{sp1}}+\left(\frac{Nr_{\mathrm{br}}^2\cos\alpha}{I_{\mathrm{cp}}}+\frac{r_{\mathrm{bp}}^2}{I_{\mathrm{p1}}}\right)\frac{c_{\mathrm{rp1}}}{\omega_0}\dot{\bar{x}}_{\mathrm{rp1}}\\
&\quad+\left(\frac{r_{\mathrm{br}}r_{\mathrm{bs}}}{I_{\mathrm{cp}}}-\frac{r_{\mathrm{bp}}^2}{I_{\mathrm{p1}}}\right)\frac{\bar{k}_{\mathrm{sp1}}}{b_0\omega_0^2}(\tau)f(\bar{x}_{\mathrm{sp1}})+\left(\frac{r_{\mathrm{br}}^2\cos\alpha}{I_{\mathrm{cp}}}+\frac{r_{\mathrm{bp}}^2}{I_{\mathrm{p1}}}\right)\frac{\bar{k}_{\mathrm{rp1}}}{b_0\omega_0^2}(\tau)f(\bar{x}_{\mathrm{rp1}})\\
&\quad+\frac{(N-1)r_{\mathrm{br}}r_{\mathrm{bs}}}{I_{\mathrm{cp}}}\cdot\frac{\bar{k}_{\mathrm{sp1}}}{b_0\omega_0^2}(\tau)f\left(\bar{x}_{\mathrm{sp1}}+\frac{r_{\mathrm{bs}}\Delta\theta_{\mathrm{f}}}{b_0}\right)+\frac{(N-1)r_{\mathrm{br}}^2\cos\alpha}{I_{\mathrm{cp}}}\frac{\bar{k}_{\mathrm{rp1}}}{b_0\omega_0^2}(\tau)f\left(\bar{x}_{\mathrm{rp1}}-\frac{r_{\mathrm{br}}\Delta\theta_{\mathrm{f}}}{b_0}\right)\\
&\quad+\left(\frac{(N-1)r_{\mathrm{br}}r_{\mathrm{bs}}^2c_{\mathrm{sp1}}}{I_{\mathrm{cp}}}-\frac{(N-1)r_{\mathrm{br}}^3c_{\mathrm{rp1}}\cos\alpha}{I_{\mathrm{cp}}}\right)\frac{\Delta\dot{\theta}_{\mathrm{f}}}{\omega_0^2}-\frac{r_{\mathrm{br}}T_{\mathrm{L}}}{I_{\mathrm{cp}}b_0\omega_0^2}+\frac{r_{\mathrm{br}}\Delta\ddot{\theta}_{\mathrm{f}}}{\omega_0^2}-\frac{\ddot{e}_{\mathrm{rp1}}(\tau)}{\omega_0^2}
\end{cases}
\tag{21}
$$

where

$$
\begin{cases}
\bar{k}_{\mathrm{sp}i}(\tau)=k_{\mathrm{sp}}\left[1+\frac{2k_{\mathrm{s}}}{\pi}\sin(\bar{\omega}\tau)+\frac{2k_{\mathrm{s}}}{3\pi}\sin(3\bar{\omega}\tau)+\frac{2k_{\mathrm{s}}}{5\pi}\sin(5\bar{\omega}\tau)\right]\\
\bar{k}_{\mathrm{rp}i}(\tau)=k_{\mathrm{rp}}\left[1+\frac{2k_{\mathrm{r}}}{\pi}\sin(\bar{\omega}\tau)+\frac{2k_{\mathrm{r}}}{3\pi}\sin(3\bar{\omega}\tau)+\frac{2k_{\mathrm{r}}}{5\pi}\sin(5\bar{\omega}\tau)\right]
\end{cases}
\tag{22}
$$

$$
\begin{cases}
\bar{e}_{\mathrm{sp}i}(\tau)=\frac{E_{\mathrm{sp}i}}{b_0}\sin(\bar{\omega}\tau+\varphi_{\mathrm{sp}i})\\
\bar{e}_{\mathrm{rp}i}(\tau)=\frac{E_{\mathrm{rp}i}}{b_0}\sin(\bar{\omega}\tau+\varphi_{\mathrm{rp}i})
\end{cases}
\tag{23}
$$

$$
f(\bar{x})=\begin{cases}\bar{x}-1 & \bar{x}>1\\ 0 & |\bar{x}|\leqslant 1\\ \bar{x}+1 & \bar{x}<-1\end{cases}
\tag{24}
$$

All the derivations here are calculated with respect to the dimensionless time τ. Eq. (21) is the dimensionless nonlinear dynamic model of a cracked planetary gear train. When $l=0$, then $\Delta\theta_{\mathrm{f}}=0$, and Eq. (21) becomes a crack-free dynamic model.

4. Comparison, solution and validation

4.1. Comparison

The predictions from a nonlinear dynamic model of Alshyyab and Kahraman[19] are used to validate the model proposed in this paper. The validation will be done by comparing the calculation with that of MHBM and of CDM.[19] Parameters of the example gear train are shown in Table 5.

In order to compare the model predictions with the earlier predictions[19], dimensionless dynamic mesh forces along the action lines are also expressed as

$$
\begin{cases}
\bar{F}_{\mathrm{sp}}=\sum_{i=1}^{N}(\bar{K}_{\mathrm{sp}i}+\bar{C}_{\mathrm{sp}i})=\sum_{i=1}^{N}[\bar{k}_{\mathrm{sp}}(\tau)f(\bar{x},B_{\mathrm{sp}i})+c_{\mathrm{sp}i}\dot{\bar{x}}_{\mathrm{sp}i}]\\
\bar{F}_{\mathrm{rp}}=\sum_{i=1}^{N}(\bar{K}_{\mathrm{rp}i}+\bar{C}_{\mathrm{rp}i})=\sum_{i=1}^{N}[\bar{k}_{\mathrm{rp}}(\tau)f(\bar{x},B_{\mathrm{rp}i})+c_{\mathrm{rp}i}\dot{\bar{x}}_{\mathrm{rp}i}]
\end{cases}
\tag{25}
$$

And the comparisons of $\bar{F}_{\mathrm{sp}}$ and $\bar{F}_{\mathrm{rp}}$ are shown in Fig. 10, respectively.

Table 5 Parameters of example planetary gear train (using nonlinear dynamic model[19]).

Parameter	Sun gear	Planet gear	Ring gear
Number of teeth	34	18	70
Module (mm)	1.5	1.5	1.5
Pressure angle (°)	21.3	21.3	21.3
Circular tooth thickness (mm)	1.895	2.585	1.844
Face width (mm)	30	30	30
Root radius (mm)	23	11.875	55

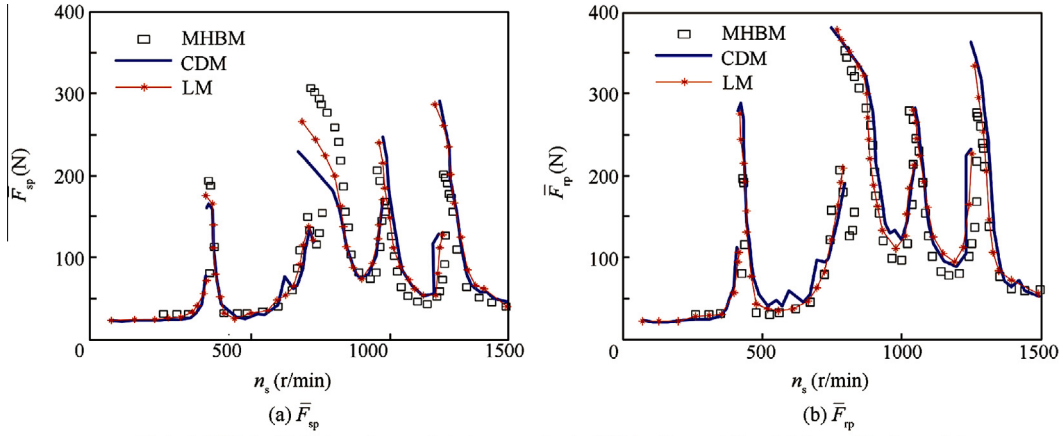

(a) $\bar{F}_{\mathrm{sp}}$ (b) $\bar{F}_{\mathrm{rp}}$

Note: MHBM—Multi-term harmonic balance method; CDM—Computational deformed-body model; LM—Lagrange method (proposed in this paper)

Fig. 10 $\bar{F}_{\mathrm{sp}}$ and $\bar{F}_{\mathrm{rp}}$ predictions of three methods.

In the calculation for comparison, several changes such as $N = 4$ and $l = 0$ mm are made to fit the comparison.

The solution values for $\bar{F}_{sp}$ and $\bar{F}_{rp}$ for three different methods (MHBM, LM, and CDM) are presented in Fig. 10. The results are for the sun gear speed range of 0–15000 r/min. In Fig. 10, $\bar{F}_{sp}$ and $\bar{F}_{rp}$ predictions of LM (proposed in this paper) are in good agreement with the CDM as well as MHBM. Not only the resonant peak frequencies but also the overall shape of the response curve agree well. And also, the jump discontinuities and typical softening type behavior are in close agreement. Although employing several simplifying assumptions, comparisons show that the dynamic model proposed in this paper is accurate in predicting $\bar{F}_{sp}$ and $\bar{F}_{rp}$.

4.2. Solution and discussion

In this section, Eq. (21) is solved numerically to demonstrate the validity and accuracy of the dynamic model. The parameters of the example gear train and other key parameters used in the calculation are given in Tables 6 and 7.

Table 6 Parameters of example planetary gear train.

Parameter	Sun gear	Planet gear	Ring gear
Number of teeth	38	47	132
Module (mm)	2.75	2.75	2.75
Pressure angle (°)	20	20	20
Face width (mm)	44	44	55
Base circle radius (mm)	49	61.2	180
Number of gears	1	5	1

Table 7 Other key parameters used in calculation.

Parameter	Value	Parameter	Value
$k_{sp1}(10^9$ N/m)	0.88	E_{spi} $(10^{-5}$ m)	1.0
$k_{rp1}(10^9$ N/m)	1.1	E_{rpi} $(10^{-5}$ m)	1.0
$c_{sp1}(10^3)$	4.66	B_{spi} $(10^{-5}$ m)	1.0
$c_{rp1}(10^3)$	6.978	B_{rpi} $(10^{-5}$ m)	1.0
e	0.03	γ	1.58
k^0 (kN/mm ·mm)	14		

Vibration signals in both time and frequency domains are obtained from the solutions of the dynamic equations (see Figs. 11 and 12).

Fig. 11 shows the time domain vibration signals of the two gear pairs (sun/planet and ring/planet) simulated by the dynamic model (50% torque and moderate crack fault). Each period of carrier rotation has five peaks corresponding to five planet gears. It can be seen clearly that sharp changes occur when Planet gear 1 (with a crack on the root of mounting Post 1) passes by the virtual sensor. In the sun gear vibration curve (see Fig. 11(a)), there is an apparent decrease in amplitude, as well as an increase in ring gear vibration curve (see Fig. 11(b)). Fig. 12 shows a series of vibration curves of sun gear and ring gear in frequency domain respectively. The carrier rotation frequency and gear meshing frequency are quite prominent in this figure. Asymmetrical sideband components, resulting from sidebands suppression and modulation, are also visible around the two key frequencies.

Amplitudes of Planet gear 1 in two gear pairs (sun/planet and ring/planet) with different carrier crack lengths with several different torque values are presented in Fig. 13.

Fig. 13 show that once a crack occurs at a carrier plate post, the sun gear vibration amplitude will sharply decrease, due to the local stiffness variation around the crack; while the amplitude of ring gear vibration will increase as the crack length increases, no matter how the torque changes. Tendencies of vibration amplitude variations become more apparent when curves of different torques are overlaid on the single figure (see Fig. 14).

Feature curves in Fig. 14 reveal the trends of vibration amplitudes caused by Planet gear 1 (at 5 multiples of carrier rotation frequency) in two gear pairs which vary with respect to the crack length under different torques. The feature curve of sun gear does not vary linearly with respect to the crack length, however, that of ring gear varies linearly.

Furthermore, the total response of the gearbox will be more valuable in application. As shown in Fig. 15, the total response curve is obtained by adding the vibration amplitude of sun gear to that of ring gear, as both of them are induced by the crack fault, and have the same feature frequency, 5 multiples of carrier rotation frequency.

Curves in Fig. 15 show good linearity not only with respect to crack length, but also to torque values. Based on this, the

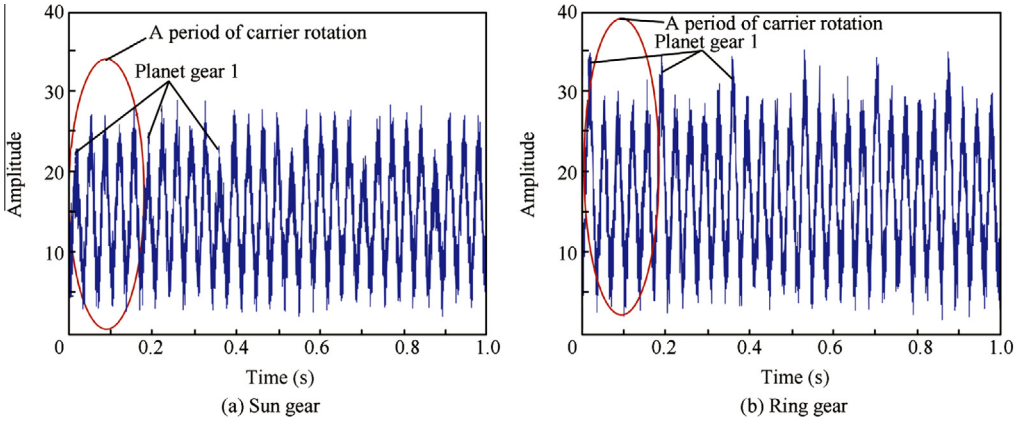

Fig. 11 Vibration signal of sun gear and ring gear in time domain (50% torque and moderate crack fault).

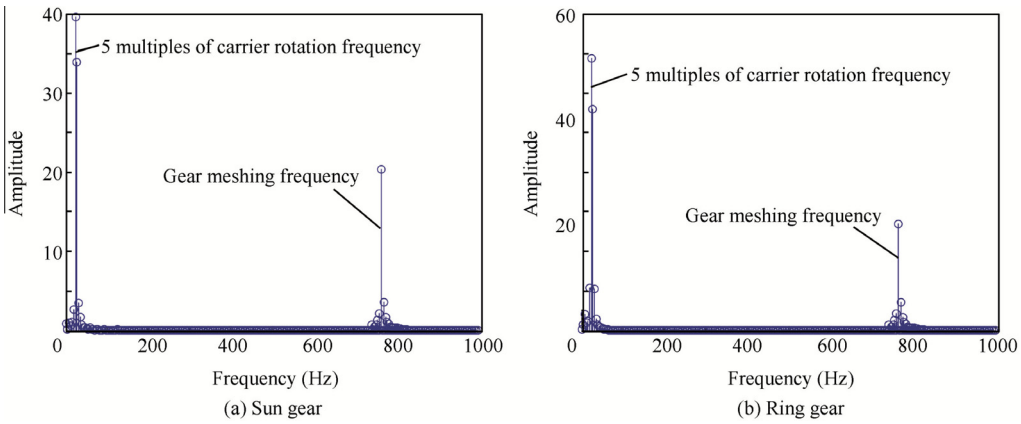

Fig. 12 Vibration curves of sun gear and ring gear in frequency domain (50% torque and moderate crack fault).

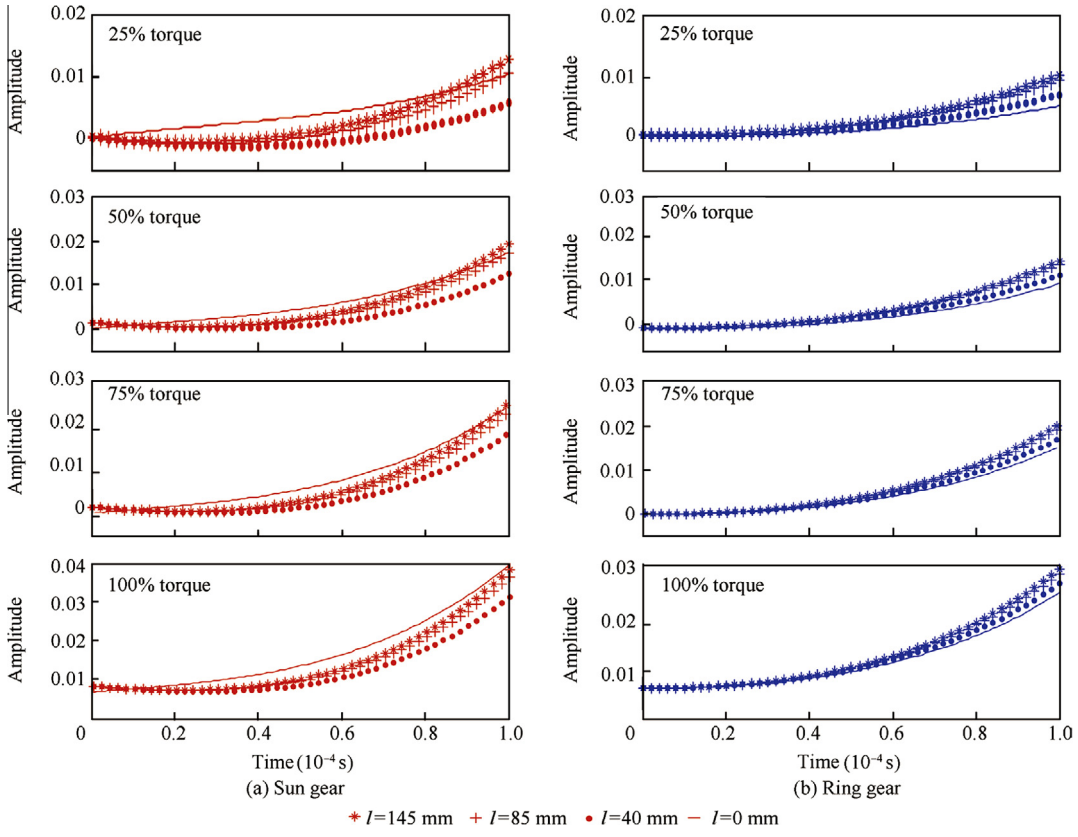

Fig. 13 Gear pairs vibration caused by Planet gear 1.

amplitude of total response at 5 multiples of carrier rotation frequency can be chosen as the feature value for the diagnosis of the crack fault in a planetary carrier plate.

4.3. Validation

An ANSYS® Workbench (AW) simulation is chosen as a comparison with the prediction of the dynamic model proposed in this paper, because some restrictions make experiment not be completed temporarily. In mechanical engineering, random vibration is motion which is non-deterministic, meaning that future behavior cannot be precisely predicted. The randomness is not the mode shapes or natural frequencies, but a characteristic of the excitation or input. ANSYS® Workbench random vibration analysis enables researchers to determine the response of structures to vibration loads that are random in nature. In this paper, a random vibration analysis is carried out to simulate the response of cracked planetary gear train to the gears meshing vibration excitation. The simulation conditions are shown in Table 8.

The random vibration analysis is carried out with software ANSYS® Workbench and the total response amplitude at 5 multiples of carrier rotation frequency is obtained. A comparison between the prediction of the dynamic model and that of ANSYS® Workbench is illustrated in Fig. 16.

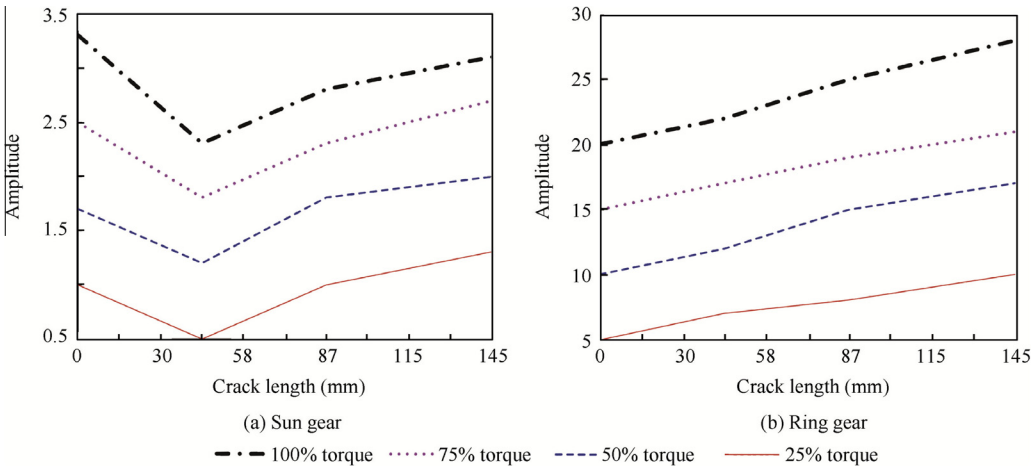

Fig. 14 Feature curves of crack fault.

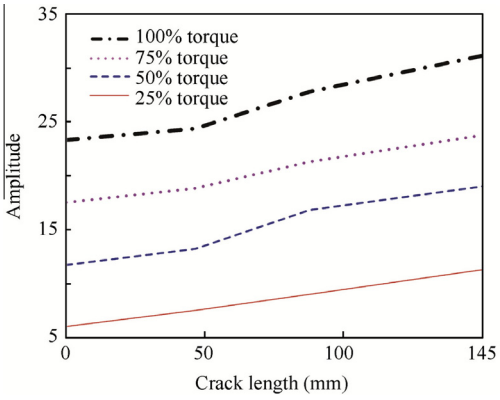

Fig. 15 Total response curve.

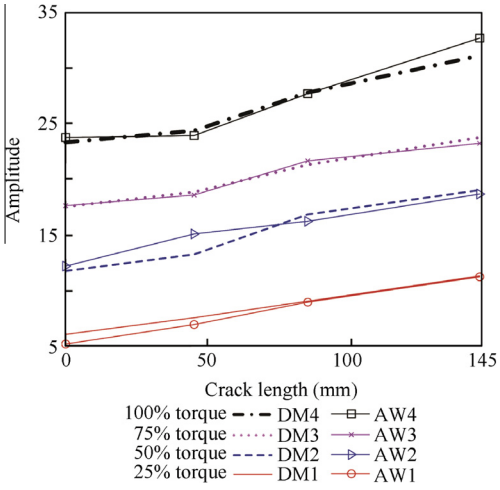

Fig. 16 Prediction comparison between dynamic model (DM) and ANSYS® Workbench (AW).

Table 8 ANSYS® Workbench simulation conditions.

Parameter	Value
Software	ANSYS® Workbench
Version	V15.0
Object	Planetary gear train with a cracked carrier
Analysis	Random vibration analysis
Mesh size	Default
Mesh method	Automatic
Material	Structural steel
Input	Sun gear
Output	Planetary carrier
Fixed support	Ring gear
Load torque (%)	25/50/75/100
Carrier plate rotation speed (r/min)	350
Sun gear rotation speed (r/min)	1568
Planet gear rotation speed (r/min)	982
Crack length (mm)	0–145

Fig. 16 shows the comparison between the prediction of the dynamic model and that of ANSYS® Workbench. Curves in Fig. 16 illustrate the good agreement between two value sets and the values under high torque agree with each other even better than the low torque ones.

5. Conclusions

This paper proposes a nonlinear dynamic model to simulate torsional vibration of a planetary gear train with a cracked planet carrier plate. The model takes into consideration nonlinear factors such as the time-varying meshing stiffness, gear backlash, viscous damping, and angular shift of posts, in simulating the effects of a planet carrier plate crack on the dynamic characteristics of the planetary gear train. Comparison of model behavior with reference data shows good accuracy of the model for predicting dynamic characteristics of a planetary gear train. The research results indicate that vibration signals of both gear pairs (sun/planet and ring/planet) in dynamic model exhibit noticeable variations in amplitudes at the cracked post (Post 1 in this paper). The signals of crack are apparent and easily detectable in both time and frequency domains. Fault features extracted from these variations indicate the length and location of a planet carrier crack clearly.

The research also finds that asymmetrical sideband components occur in proximity to the carrier rotation frequency as well as meshing frequency. Their effect is not clear and a comprehensive investigation on that topic is scheduled to be part of the future work.

Acknowledgements

The authors are grateful to Prof. Tomovic for discussions, KONG Dehe and XU Guanfeng for providing data. This paper was co-supported by the National Basic Research Program of China (2014CB046402), the Natural Science Foundation of China (Grant No. 51175014) and "111" Project.

References

1. Blunt DM, Keller JA. Detection of a fatigue crack in a UH-60A planet gear carrier using vibration analysis. *Mech Syst Signal Process* 2006;**20**(8):2095–111.
2. Wu BQ, Saxena A, Patrick R, Vachtsevanos G. Vibration monitoring for fault diagnosis of helicopter planetry gears. *Proceedings of 16th IFAC world congress*; 2005 July 4–8; Prague, Czech Republic. Amsterdam: Elsevier; 2005. p.1–6.
3. Saxena A, Wu BQ, Vachtsevanos G. A methodology for analyzing vibration data from planetary gear systems using complex morlet wavelets. *2005 American control conference*; 2005 June 8–10; Portland (OR). Piscataway (NJ): IEEE; 2005. p. 4730–5.
4. Sparis P, Vachtsevanos G. A helicopter planetary gear carrier plate crack analysis and feature extraction based on ground and aircraft tests. *International symposium on intelligent control*; 2005 June 27–29; Limassol, Cyprus.Piscataway (NJ): IEEE; 2005. p. 646–51.
5. Hou SL. Fault research of Z-9B helicopter. *Helicopter Tech* 2002 (2);40–2 [Chinese].
6. Attar M. A transfer matrix method for free vibration analysis and crack identification of stepped beams with multiple edge cracks and different boundary conditions. *Int J Mech Sci* 2012;**57** (1):19–33.
7. Wu J, Yan S, Xie L. Reliability analysis method of a solar array by using fault tree analysis and fuzzy reasoning petri net. *Acta Astronaut* 2011;**69**(11):960–8.
8. Zhang C, Wang S, Bai G. An accelerated life test model for solid lubricated bearings based on dependence analysis and proportional hazard effect. *Acta Astronaut* 2014;**95**:30–6.
9. Orchard ME, Vachtsevanos GJ. A particle-filtering approach for on-line fault diagnosis and failure prognosis. *Trans Inst Meas Control* 2009;**31**(3–4):221–46.
10. Wu BQ, Saxena A, Khawaja T, Patrick R, Vachtsevanos G. An approach to fault diagnosis of helicopter planetary gears. *Proceedings of 2004 IEEE autotestcon*; 2004 Sept. 20–23; San Antonio (TX). Piscataway (NJ): IEEE; 2004. p.475–81.
11. Patrick R, Orchard ME, Zhang B. An integrated approach to helicopter planetary gear fault diagnosis and failure prognosis. *Proceedings of 2007 IEEE autotestcon*; 2007 Sept. 17–20; Baltimore (MD). Piscataway (NJ): IEEE; 2007. p. 547–52.
12. Feng Z, Liang M, Zhang Y, Hou S. Fault diagnosis for wind turbine planetary gearboxes via demodulation analysis based on ensemble empirical mode decomposition and energy separation. *Renewable Energy* 2012;**47**:112–26.
13. Lei Y, Kong D, Lin J, Zuo MJ. Fault detection of planetary gearboxes using new diagnostic parameters. *Meas Sci Technol* 2012;**23**(5):1–10.
14. Ma H, Pang X, Feng R, Song R, Wen B. Fault features analysis of cracked gear considering the effects of the extended tooth contact. *Eng Fail Anal* 2015;**48**:105–20.
15. McFadden PD, Smith JD. An explanation for the asymmetry of the modulation sidebands about the tooth meshing frequency in epicyclic gear vibration. *Arch Proc Inst Mech Eng C J Mech Eng Sci 1989-1996 (vols. 203–210)* 1985;**199**(13):65–70.
16. Sun T, Shen YW, Sun ZM, Liu JY. Study on nonlinear dynamic behavior of planetary gear train solution and dynamic behavior analysis. *Chin J Mech Eng* 2002;**38**(3):11–6 [Chinese].
17. Sun T, Shen YW, Sun ZM, Liu JY. Study on nonlinear dynamic behavior of planetary gear train dynamic model and governing equations. *Chin J Mech Eng* 2002;**38**(3):6–11 [Chinese].
18. Sun ZM, Ji LH, Shen YW. Nonlinear dynamics of 2K-H planetary gear train. *J Tsinghua Univ (Sci Technol)* 2003;**43**:636–9 [Chinese].
19. Alshyyab A, Kahraman A. A non-linear dynamic model for planetary gear sets. *Proc Inst Mech Eng Part K: J Multi-body Dyn* 2007;**221**(4):567–76.
20. Yuksel C, Kahraman A. Dynamic tooth loads of planetary gear sets having tooth profile wear. *Mech Mach Theory* 2004;**39** (7):695–715.
21. Cheng Z, Hu NQ, Qin GJ. Quantitative detection approach for transmission system of helicopter based on physical model and gray relational analysis. *J Aerosp Power* 2011;**26**(03):716–20 [Chinese].
22. Feng Z, Zuo MJ. Vibration signal models for fault diagnosis of planetary gearboxes. *J Sound Vib* 2012;**331**(22):4919–39.
23. Liang XH, Zuo MJ, Pandey M. Analytically evaluating the influence of crack on the mesh stiffness of a planetary gear set. *Mech Mach Theory* 2014;**76**:20–38.
24. Liang X, Zuo MJ, Hoseini MR. Vibration signal modeling of a planetary gear set for tooth crack detection. *Eng Fail Anal* 2015;**48**:185–200.
25. Patrick-Aldaco R. A model based framework for fault diagnosis and prognosis of dynamical systems with an application to helicopter transmissions[dissertation]. Georgia: Georgia Institute of Technology, 2007.
26. Rao SS. *Mechanical vibrations*. 5th ed. Singapore: Pearson/Prentice Hall; 2011, p. 1105.
27. China State Bureau of Technical Supervision. Calculation methods of load capacity for involute cylindrical gears. Beijing: Chinese Ministry of Machine-Building Industry; 1997. p. 81. [Chinese].
28. Li RF, Wang JJ. *Gear system dynamics-vibration, shock and noise*. Beijing: Science Press; 1997. p. 69–97 [Chinese].

Fan Lei is a Ph.D. candidate at School of Automation Science and Electrical Engineering, Beihang University. He received his M.E. degree from PLA University of Science and Technology in 2011. His area of research includes reliability and fault diagnosis.

Wang Shaoping is a professor and Ph.D. supervisor of School of Automation Science and Electrical Engineering, Beihang University. She received the B.S., M.S. and Ph.D. degrees in mechatronic engineering from Beihang University in 1988, 1991 and 1994 respectively. Her main research interests are mechatronic control, reliability and fault diagnosis.